Quantum Time Transfer: A Practical Method for Lossy and Noisy Channels

Randy Lafler[*] and R. Nicholas Lanning

Air Force Research Laboratory, Directed Energy Directorate, Kirtland AFB, New Mexico, USA

Timing requirements for long-range quantum networking are driven by the necessity of synchronizing the arrival of photons, from independent sources, for Bell-state measurements. Thus, characteristics such as repetition rate and pulse duration influence the precision required to enable quantum networking tasks such as teleportation and entanglement swapping. Some solutions have been proposed utilizing classical laser pulses, frequency combs, and biphoton sources. In this article, we explore the utility of the latter method since it is based upon quantum phenomena, which makes it naturally covert, and potentially quantum secure. Furthermore, it can utilize relatively low performance quantum-photon sources and detection equipment, but provides picosecond-level timing precision even under high loss and high noise channel conditions representative of daytime space-Earth links. Therefore, this method is relevant for daytime space-Earth quantum networking and/or providing high-precision secure timing in global positioning system–denied environments.

I. INTRODUCTION

Precise synchronization of remote clocks is at the heart of position, navigation, and timing, high-speed transactions, distributed computing, and as of late, quantum networking. To enable *global-scale* quantum networking, one needs to distribute entanglement between distant quantum nodes [1,2], which will likely require a series of entanglement swapping operations between different arrangements of ground and satellite quantum nodes [3,4]. If ultranarrow spectral filtering is utilized then each entanglement swapping operation could require Bell-state measurements with as little as nanosecond-scale timing precision. This can be achieved utilizing single-photon avalanche-diode (SPAD) detectors and synchronization provided by current global positioning system (GPS) public signals [5]. However, ultranarrow spectral filtering is not currently compatible with entangled photon sources, which are generally broader band, and would result in considerable attenuation. An alternate approach is to increase the timing precision to the picosecond or femtosecond level, along with choosing the appropriate pulse duration and spectral-temporal filtering. This would result in a higher probability of success per pulse and maintain the rejection of noise photons that scatter into the channel. Therefore, techniques to precisely synchronize remote clocks are an important ongoing area of research.

Perhaps the most straightforward optical-time-transfer technique uses laser pulses, photodetectors, and software-based correlation methods. For example, time transfer by laser link (T2L2) demonstrations have achieved picosecond-scale precision between remote ground stations operating in common view with the Jason-2 satellite [6]. In contrast, there are also hardware-based methods such as optical two-way time and frequency transfer (O-TWTFT) [7,8], which utilizes frequency combs and linear optical sampling to synchronize two remote clocks to femtosecond precision. Demonstrations of O-TWTFT have been performed between stationary sites [7,8] or slow moving drones, < 25 m/s. The conclusions in Refs. [9,10] suggest that O-TWTFT can maintain femtosecond-scale precision despite the high orbital velocities and nonreciprocity of two-way Earth-satellite links, but a demonstration over channel conditions representative of an Earth-satellite link has yet to be performed.

The concept of using quantum phenomena has also emerged as a possible solution for precise synchronization. One example is the Earth-satellite synchronization demonstration that used quantum key distribution (QKD) with attenuated laser pulses and a high powered sync pulse [11]. However, this technique relies on extraneous components and classical pulsing, making it more complex and less covert. Another example relies on Hong-Oh-Mandel quantum interference between entangled photon pairs [12]. However, it is challenging to utilize this technique over freespace-atmospheric channels due to aberrations of the photon transverse momentum and the very high level of attenuation characteristic of the double-pass geometry.

---

*AFRL.RDSS.OrgMailbox@us.af.mil

Another technique consists of utilizing the femtosecond-scale temporal correlations of photon pairs created in spontaneous-parametric down-conversion (SPDC) photon sources [13] and has recently been considered for global-scale networks [14]. In this case, the relative time offset between two remote clocks is measured with the following procedure: (1) a series of photon pairs are separated and transmitted to two remote sites, (2) the photons are detected and time tagged based on the respective local clock, (3) after enough detection events are collected, the series of arrival times from each site are combined and correlation methods are used to find the clock offset. This technique was demonstrated in Refs. [13,15,16] and it is referred to as quantum time transfer (QTT) for the remainder of this paper. One-way QTT [15] can provide relative clock synchronization and two-way QTT [16] can provide absolute clock synchronization.

One can think of QTT as a quantum analog of T2L2, where the laser pulses of T2L2 are replaced with randomly arriving, but correlated, photon pairs. A continuous-wave (cw) biphoton source creates pairs that are distributed randomly over the acquisition time. Therefore, correlating the signals with QTT reveals a single peak corresponding to the clock offset, whereas deterministic pulsing results in a collection of peaks repeating at the pulse period. It is possible to perform QTT using pulsed-biphoton sources, provided the photon pairs are still created *probabilistically*. The key requirement is that some of the pulses must be empty and Alice must register that information. For pulsed-biphoton sources that are probabilistic, one typically keeps the probability of pair creation per pulse low in order to suppress multipair events. This results in many empty pulses, and the coincidence peak corresponding to the clock offset will be larger than the peaks corresponding to the pump-pulse cycle. Similarly, the algorithm will work for weak-coherent-pulse quantum-key-distribution photon sources, provided that enough random vacuum-decoy pulses are used to suppress the side peaks.

In this article, we propose a simple and computationally fast method of QTT and investigate the cw biphoton-source approach. In Sec. II we introduce a potential freespace architecture, outline the algorithm, and discuss the expected precision. In Sec. III we assume several different heralding efficiency sources and perform a simulation spanning a large space of channel attenuation and noise-photon rates. We consequently discuss the probability of success per acquisition, the standard error of the mean of the measured clock offset, and the overlapping Allan deviation, which conveys the stability and noise profile of the two-clock system. In Secs. IV and V we interpret the results in the context of fiber channels and space-to-Earth downlinks with sky-noise photons and slant-path turbulence, thereby demonstrating the relevance of this method for global-scale quantum networking.
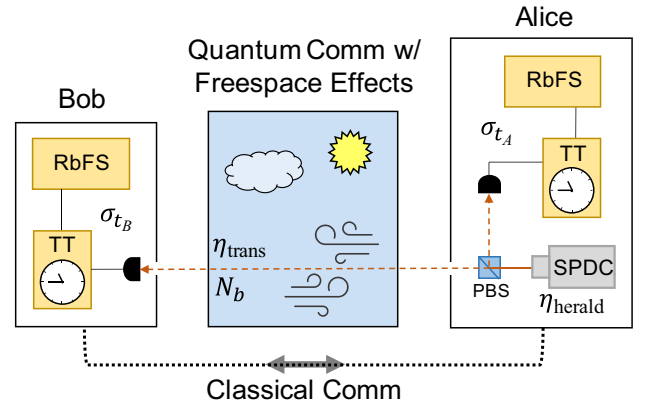

FIG. 1. Diagram of relevant components and phenomena present when performing QTT over daytime atmospheric channels. Alice uses a type-II SPDC biphoton source to create temporal correlations that facilitate QTT. She keeps one of the biphotons locally and records its detection time with a detection system consisting of a detector, a time tagger (TT), and rubidium frequency standard (RbFS), collectively with jitter σ_{t_A}. With heralding efficiency η_{herald}, she sends the companion photon to Bob who similarly records the detection event, subsequent to his total channel attenuation, which includes the atmospheric transmission η_{trans} [see Eq. (2)]. The atmosphere also causes sky noise photons N_b to scatter into the channel. Bob announces the time tags over a classical channel and Alice uses this information to perform a correlation measurement to determine the relative clock offset τ.

II. QUANTUM TIME TRANSFER

A. Example architecture

QTT has several advantages over the aforementioned techniques that make it promising for *freespace* channels. Namely, the architecture is relatively simple, low size, weight, and power, and the algorithm is robust to loss and noise photons. Figure 1 depicts some of the relevant components and phenomena comprising QTT over daytime-freespace channels. We assume for the moment that Alice and Bob both utilize SPAD detectors, time-tagging units, and rubidium frequency standards to provide initial system stability, which is discussed more in the following subsection. Alice records one of the biphotons locally subsequent to spectral, detector, and heralding efficiencies

$$\eta_A = \eta_{\text{spec}}\eta_{\text{det}}\eta_{\text{herald}}. \tag{1}$$

Bob similarly records detection events with extra attenuation imposed by the optical receiver and the atmospheric effects

$$\eta_B = \eta_{\text{ch}}\eta_{\text{herald}}, \tag{2}$$

where $\eta_{\text{ch}} = \eta_{\text{spec}}\eta_{\text{det}}\eta_{\text{rec}}\eta_{\text{trans}}$ is Bob's channel attenuation. Background-noise photons N_b, which can be calculated using radiometric equations [17], scatter to Bob's
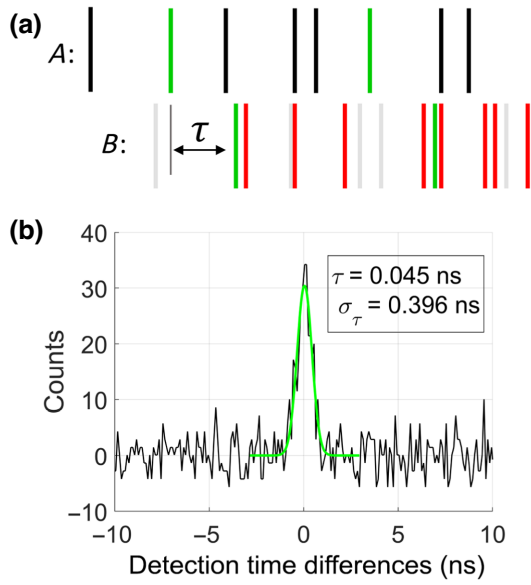
FIG. 2. (a) Data stream depicting the phenomena underpinning QTT. Alice records a stream of detection events represented by the time tags (see the top row). Bob records the same events as Alice with efficiency η_B (see the bottom row). In Bob's stream, potential detection events that are lost are grayed out, and events corresponding to background-noise photons are colored red. The infrequent true coincidences that give rise to a correlation peak at τ are colored green. (b) An example correlation histogram (black curve). The green curve is a Gaussian fit of the correlation peak, which establishes the clock offset τ and its standard deviation σ_τ resulting from the total systematic detection time jitter (see Sec. II C).

detector subsequent to attenuation $\eta_{\rm spec}\eta_{\rm det}\eta_{\rm rec}$. Figure 2(a) shows the effect of these phenomena on the time series of detection events registered by Bob. Alice records a stream of detection events represented by the time tags in the top row. Bob records the same events as Alice with efficiency η_B. In Bob's stream, potential detection events that are lost are grayed out, and events corresponding to background-noise photons are colored red. The infrequent true coincidences that give rise to a correlation signal at the clock offset τ are colored green.

B. Algorithm

The QTT algorithm presented in Ref. [15] measures the total clock offset τ with a series of increasingly precise cross-correlations. Their algorithm can be summarized as follows. First, judiciously choose an acquisition time depending on the rate of Alice's and Bob's detection events and divide it into an empty array of N bins of width w, one array each for Alice and Bob. Second, for each array, assign a 1 to every bin where a time tag is present and a 0 otherwise. Third, calculate the discrete cross-correlation of the arrays to find a peak that corresponds to the relative offset between the Alice and Bob

clocks. The algorithm can be repeated again with a narrower bin width to increase the measurement precision, but it is very sensitive to the choice of bin size, acquisition time, etc. In the regime of high channel attenuation, high background rates, and large, unknown τ, we found this algorithm to be difficult to optimize and extremely computationally intensive. This is because a very large number of bins, that is, $N > 2^{24}$ for a 1-s acquisition time, is required to isolate enough "true" coincidences from the randomly arriving background photons in order to bring the correlation peak above the noise. Nevertheless, this algorithm can be used in situations with low background rates, such as QTT in optical fiber.

In order to investigate the extreme conditions of daytime-freespace quantum links, we developed the following coincidence-finding algorithm that is based on a simple arrival-time-difference histogram. Our algorithm is quick, computationally efficient, and maintains sub-nanosecond timing precision over the parameter space we investigate in Sec. III.

(1) Concatenate the Alice and Bob time-tag arrays, t_A and t_B, respectively, and sort the resulting array M from the earliest to latest time.

(2) Find the indexes k of t_B in M, where M_k returns the array t_B of Bob's time tags.

(3) Calculate the time differences τ_{ik} between each of Bob's time tags M_k and the neighboring Alice time tags $M_{k\pm i}$ preceding and trailing each Bob time tag,

$$\tau_{ik}^{(\pm)} = M_{k\pm i} - M_k, \qquad (3)$$

where index i goes from 0 to an upper limit n, which must be large enough to contain the offset.

(4) Histogram the resulting time differences τ_{ik} with bin size $T_{\rm bin}$ over a range large enough to include the expected clock offset.

(5) When the algorithm is successful, there is a Gaussian feature in the histogram with mean corresponding to the relative clock offset τ and standard deviation σ_τ corresponding to the system jitter.

QTT can be used as a stand-alone protocol, or to underpin other quantum protocols, such as entanglement-based QKD or entanglement distribution. In the latter case, one would want to find and isolate the coincidence detection events from the background, and use them for further processing. To do this, Bob adjusts his time tags t_B according to

$$t'_B = (t_B + \tau) \times (1 + \Delta U), \qquad (4)$$

where ΔU is the clock drift estimated by subtracting successive clock offset measurements τ_i and dividing by the

acquisition time,

$$\Delta U = \frac{\tau_{i+1} - \tau_i}{T_a}. \tag{5}$$

The procedure outlined in this section, culminating in Eq. (4), is a relative clock synchronization since the time of flight of the photons between Alice and Bob is not known with high precision. If instead one performs QTT in both directions, that is, two-way QTT, the propagation time can be measured and the clocks can be synchronized absolutely [16].

C. Precision

Our QTT algorithm generates a Gaussian correlation feature with mean equal to the clock offset τ and standard deviation σ_τ. Consequently, the central limit theorem suggests that the uncertainty of our clock offset measurement τ is

$$\sigma_{\bar{\tau}} = \sigma_\tau / \sqrt{N_{\mathrm{T}}}, \tag{6}$$

where, for the remainder of the paper, we refer to $\sigma_{\bar{\tau}}$ as the standard error of the mean (SEM), $N_{\mathrm{T}} = N_{\mathrm{C}} - N_{\mathrm{AC}}$ is an estimate of the number of true coincidences, N_{C} is the number of measured coincidences, and N_{AC} is an estimate of the number of accidental coincidences. The standard deviation of the correlation σ_τ is primarily a measure of the systematic timing error of all the detection components in the system

$$\sigma_t^{(\mathrm{sys})} = \sqrt{\sigma_{t_A}^2 + \sigma_{t_B}^2}, \tag{7}$$

where σ_{t_A} and σ_{t_B} are the timing jitters of Alice's and Bob's systems, respectively.

In Fig. 2(b) we present an example correlation motivated by challenging channel conditions and timing jitter observed in our testbed [18]. Namely, we assume a 2-MHz biphoton source rate, channel attenuation $\eta_{\mathrm{ch}} = -23$ dB, background photons $N_b \approx 9 \times 10^5$, and a total system jitter $\sigma_t^{(\mathrm{sys})} = 405$ ps. From the Gaussian fit we see that $\sigma_\tau = 396$ ps, which is consistent with the systematic jitter $\sigma_t^{(\mathrm{sys})}$ within the fitting errors. In fact, the correlation width is characteristic of the system and is relatively unchanged regardless of the channel conditions. Therefore, the width of the correlation feature can be used as a test to determine if the algorithm was successful. For example, if QTT and the peak-finding algorithm obtain a noise peak then the width would likely be much narrower than a true peak, and the erroneous τ could be disregarded. We use this technique in finding the probability of success in Sec. III F.

III. SIMULATION

A. Clock offset

In principle, the performance of QTT is unaffected by the value of the clock offset, assuming that the range of the correlation histogram is large enough to include it. However, in practice, measuring large clock offsets could require a prohibitively large amount of computation time unless treated properly. For example, measuring a 1-s clock offset with 100-ps bins would require the correlation histogram to have at least 10^{10} bins. Therefore, in practice one divides large clock offsets into coarse and fine components [13], and if available, one can use GPS or estimates of the propagation time to narrow the searching space. Since we are interested in the fundamental performance of the QTT algorithm, we consider only the fine component of the clock offset τ, and without loss of generality, we let $\tau = 0$.

B. Clock drift

The observed frequency drift between Alice's and Bob's clocks ΔU can be caused by clock drift or relative motion. For systems with large clock drift ΔU, it is important to model ΔU and preemptively subtract it from the measured time series using Eq. (4). For example, it is common practice for GPS and laser-communication systems to model and remove the effects of Doppler shift, gravitational frequency shift, and other effects in order to prevent large timing errors [19]. Consequently, we omit the effects due to relative motion. In other words, we assume that course clock drift correction has been performed and study the performance of QTT subject to the clock drift ΔU contributions that are inherent to the QTT system. This includes modeling errors and frequency jitter, which we assume to be a Gaussian-distributed random variable with zero mean and standard deviation σ_U. We discuss how the remaining ΔU contributions can negatively impact performance and limit the acquisition time T_a in Appendix A 1. We consider three different clock stabilities: rubidium frequency standards (RbFSs), cesium frequency standards (CsFSs), and perfectly stable clocks (that is, $\sigma_U = 0$). For the RbFS case, we performed QTT in our testbed and measured $\Delta U = 3.4 \times 10^{-10}$ and frequency jitter $\sigma_U = 3 \times 10^{-12}$. For the CsFS case, we used the same ΔU but $\sigma_U = 5 \times 10^{-13}$ based on manufacture specifications [20,21].

C. Heralding efficiency

We investigate the performance of QTT considering sources with different heralding efficiencies. This is a pivotal consideration, because unlike sky noise photons that can be filtered with tighter spectral and spatial filtering, the photon source itself produces noise photons perfectly in band with probability $1 - \eta_{\mathrm{herald}}$. We consider four different cw sources with heralding efficiencies that range from

readily available commercial-off-the-shelf units to specialized one-off devices, namely, 20%, 40%, 60%, and 80%, respectively.

D. Photon detection statistics

1. Photon source

Photon-pair sources have different observed statistics depending on their spatiotemporal mode structure and the temporal resolution of the detection system [22]. For example, theory predicts that a single-mode biphoton source, when generalized to a two-mode squeezed vacuum state, has thermal statistics. However, this is only observed if the detection system has resolution finer than the coherence time of the photons; otherwise, Poissonian statistics are observed [23–25]. In the former case, it may be necessary to simulate thermal statistics to determine if there is a significant effect on the QTT algorithm. In this simulation, regardless of whether the source is to be considered single or multimode, the system jitter is much larger than the few picosecond coherence time of the photons assumed here. Therefore, it is sufficient to model the photon detection streams with Poisson statistics as we describe in the next section.

2. Attenuation

The phenomenon of a fluctuating atmospheric transmission, characterized by the probability distribution of the transmission coefficient, simply modulates the temporal detection signal depending on the atmospheric conditions and properties of the optical receiver system [26]. However, Eq. (3) indicates that the QTT correlation histogram is sensitive to the difference of detection times at Alice and Bob, but is insensitive to where the pairs are located in the acquisition time T_a. Consequently, modulation of the pair arrival rate during the acquisition time T_a should not impact QTT. Thus, it is sufficient to model the channel attenuation during the acquisition time T_a by a mean value.

E. Simulation methods

1. Time-tag series

We assume a cw biphoton source with a 2-MHz pair rate R and a 1-s acquisition time T_a. We assume the source generates photon pairs that obey Poisson statistics, which is equivalent to distributing the biphoton time tags randomly in T_a according to a uniform probability distribution. Therefore, each of the Alice and Bob time series are generated in the following way. First, we create an array of 2 million uniformly distributed random times between 0 and 1 s. The array is then sorted from the smallest to largest time, becoming the unattenuated Alice time series. An identical copy is made for Bob, which would be shifted appropriately relative to the Alice time series for cases where the clock offset τ is nonzero.

The effects of the total systematic timing jitter are now included by adding a Gaussian-distributed random variable with standard deviation σ_{t_A} and σ_{t_B} to each time tag of Alice's and Bob's time series, respectively. Unless otherwise noted, we assume SPAD detectors and time taggers with timing jitter $\sigma_t^{(\text{det})} = 287$ ps and $\sigma_t^{(\text{tt})} = 4$ ps, respectively. These values were chosen to match the typical timing jitters we observe with Excelitas SPCM-AQRH single-photon counting modules and PicoQuant HydraHarp 400.

Next, time tags are randomly removed from Alice's and Bob's time series equivalent to their respective channel attenuation and the heralding efficiency of the source η_{herald}. Alice's channel attenuation is set to the product of the detection efficiency $\eta_{\text{det}} = 0.6$ and the losses due to the transmission of the spectral filter $\eta_{\text{spec}} = 0.9$. Bob's channel attenuation and background-photon rate are set to span -10 to -50 dB and 0 to 800 kHz, respectively. We show that these values include conditions commensurate with a daytime space-to-Earth downlink.

2. Dead time

We include the effect of dead time, which can reduce the probability of Alice and Bob detecting true coincidences as the heralding efficiency or the background rate at Bob increases. We chose an 84-ns dead time to match the total systematic dead time that we have observed in our hardware. It is worthwhile to note that single-photon detectors can be paralyzable or nonparalyzable, which can complicate the simulation procedure. Nonparalyzable detectors are not affected by a photon that arrives during the dead time, whereas paralyzable detectors reset if a photon arrives during the dead time [27]. In this simulation, we assume a worst-case scenario by modeling paralyzable detectors and removing all time tags from Alice's and Bob's time series that are within the dead time of another time tag. However, we note that, for Bob's channel conditions assumed here, we find that the paralyzable and nonparalyzable cases give similar results.

3. After pulsing

For the components modeled in this simulation, the after pulsing probability is much less that 10^{-2} after the dead time has elapsed [28]. The number of after-pulse detection events may be numerous in practice, but they do not appreciably affect the QTT correlation signal. For example, consider a true coincidence from the correlation histogram. The probability of after pulses on Alice's *and* Bob's detectors leading to an accidental coincidence near the correlation peak is about 10^{-4}. Next, consider an after pulse on either Alice's or Bob's detector. These events are uncorrelated with the rest of the time tags in the stream. Therefore, any coincidences resulting from these time tags are randomly distributed across at least 10^9 histogram bins,
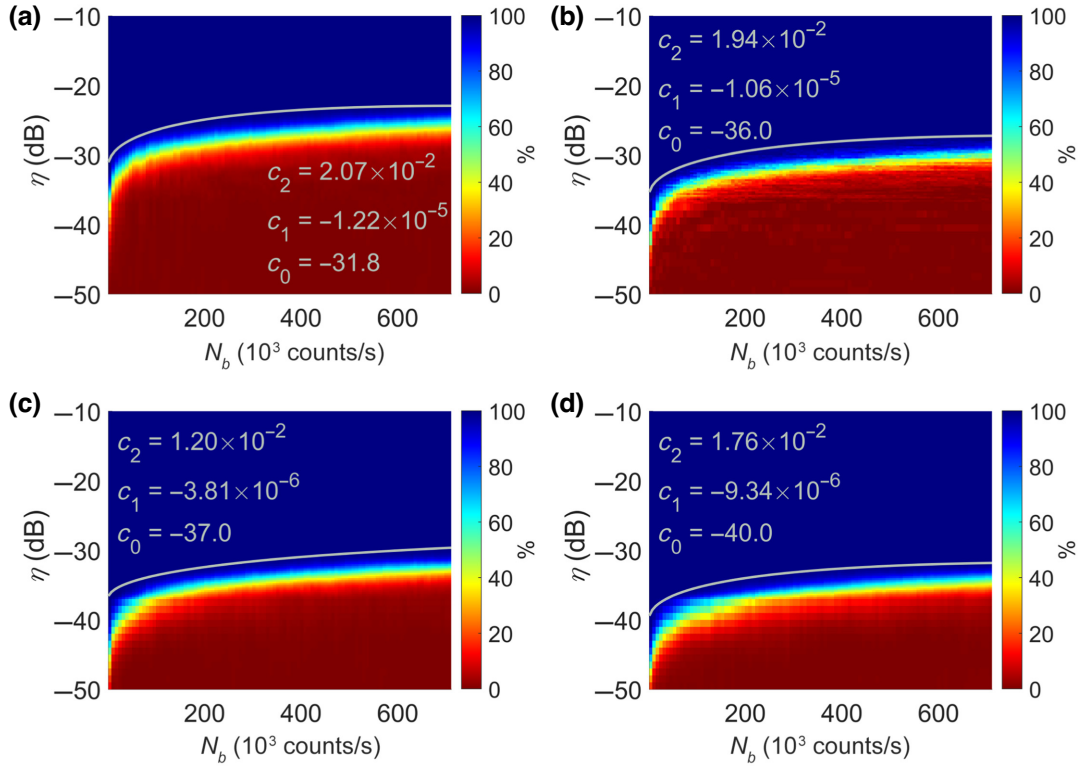
FIG. 3. Density plots giving the probability of successful QTT as a function of Bob's channel attenuation η_{ch} and background counts N_b. Panels (a)–(d) present the results for η_{herald} equal to 20%, 40%, 60%, and 80%, respectively. The gray line traces out the threshold channel attenuation that can be achieved with 99% probability of success and the inset gives the fit parameters corresponding to Eq. (A15), where c_0 is the fit parameter for the y intercept.

which leads to a negligible increase of the noise floor for this simulation space. This explains why after pulsing does not contribute significantly to the QTT algorithm and is omitted from this simulation.

4. Bin width

This concludes the preparation of Alice's and Bob's simulated time series and the QTT algorithm can now be performed. Since the clock offset τ is determined based on the mean of the Gaussian fit of the correlation peak, it is important to have a reliable fit. This translates into choosing the correlation bin size T_{bin} small enough to resolve the correlation peak, but not so small that noise fluctuations effect the fit. We find that 100- and 10-ps correlation bin widths are compatible with SPAD and superconducting nanowire single-photon (SNSPD) detectors, respectively.

F. Probability of success

In this section, we span a two-dimensional (2D) parameter space of mean channel attenuation and background-noise photons. We repeat each channel condition 100 times to find statistically relevant quantities. For each channel condition, we examine the probability of success, which is the number of times the QTT algorithm correctly identified

the clock offset in the 100 trials. Thus, the probability of success is the probability that a single instance of the QTT algorithm will return the correct clock offset. We refer to this as the "single-shot" probability of success.

In Figs. 3(a)–3(d) we show the probability of success as a function of attenuation and the number of noise photons for sources with 20%, 40%, 60%, and 80% heralding efficiencies, respectively. This shows that the QTT algorithm is highly robust to noise photons and is much more susceptible to channel loss, as seen by the abrupt drop in performance with increasing channel attenuation η_{ch}. The gray line is a fit to the 99% probability of success threshold using the framework derived in the Appendix.

G. Threshold attenuation

In Fig. 4 we impose a 99% single-shot probability of success threshold and find the corresponding channel attenuation η_{th} for 20%, 40%, 60%, and 80% heralding efficiencies. For each heralding efficiency, the marker color indicates the number of true coincidences N_T. As expected, we see that more attenuation η_{th} can be managed as the heralding efficiency increases. This is simply because higher heralding efficiencies correspond to larger true coincidence rates N_T and therefore larger coincidence
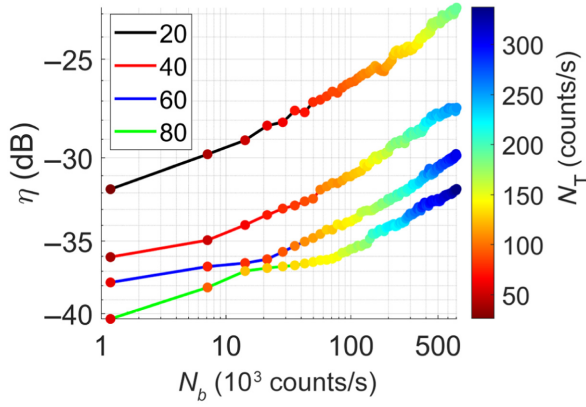
FIG. 4. Curves giving the threshold attenuation η_{th} that maintains $\geq 99\%$ probability of success as the number of sky background photons increases. The black, red, blue, and green curves correspond to 20%, 40%, 60%, and 80% heralding efficiency, respectively. The marker colors correspond to the number of true coincidences for each of the channel conditions.
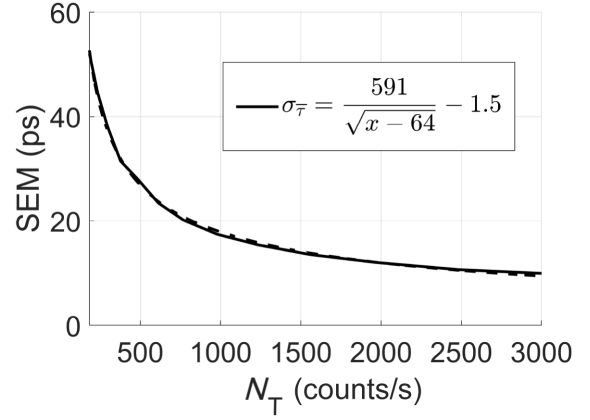

FIG. 5. The SEM clock offset as a function of the number of "true" coincidences N_T (that is, with accidentals subtracted), where the number of background photons are set to $N_b = 2 \times 10^6$ counts/s. On the black curve, each SEM is calculated by taking the standard deviation of the clock offsets measured from a Monte Carlo simulation with 1000 trials. The dashed curve is the fit and the fit parameters are given in the plot legend.

peaks. We see that the QTT algorithm achieves 99% success probability despite a 100-kHz background-photon rate and a true-coincidence rate of only a few hundred Hz. This is because the sky noise photons are uncorrelated with the true coincidences and their contribution is spread out uniformly over the entire histogram range.

H. SEM

The QTT error should converge to Eq. (6) in the limit of a large number of true coincidences (i.e., large sample size). To measure the QTT error, i.e., the *true* SEM $\sigma_{\bar{\tau}}$, we perform the following Monte Carlo simulation. First, we measure the sampling distribution by simulating 1000 independent clock offset measurements, where the background-photon rate is set at a daytime value of 2 MHz. We then measure the SEM by calculating the standard deviation of the sampling distribution. Lastly, we repeat these steps over a range of true coincidences N_T. Figure 5 gives the true SEM of the QTT algorithm, where, given the 2-MHz pair rate and 40% heralding efficiency of the source, $N_T \sim 800$ represents the expected number of true coincidences per second during a daytime space-to-Earth downlink. The fit in the inset reveals the characteristic $1/\sqrt{N_T}$ dependence of the SEM, but the numerator of the fit, 591 ps, is about 1.5 times larger than the SEM predicted by Eq. (6). If one increases N_T to large values, while also decreasing the correlation bin width T_{bin} in proportion, then the difference between the SEM calculations will tend to decrease, but only up to a limit. This is most likely related to errors incurred when fitting the correlation peak. Nevertheless, Fig. 5 shows that the timing precision of a single-shot clock offset measurement τ is proportional to $1/\sqrt{N_T}$, and the proportionality can be modeled directly depending on the source and channel conditions.

I. Allan deviation

In this section we discuss the clock stability of QTT. The Allan deviation σ_y is a standard method to characterize the stability of a clock system. When the Allan deviation is plotted on a log-log scale, the slope of the curve indicates the type of noise in the system. Thus far, we have focused on the performance of independent, single-shot QTT measurements. In order to model the stability, we simulate continuous streams of successive QTT measurements under the influence of drifting *and* jittering local clocks. The effect of clock drift and relative motion sets the mean ΔU, which we include as a modification of Bob's time series t_B according to Eq. (5). The jitter is modeled as a Gaussian random variable of standard deviation σ_U, which varies depending on the stability of the local clocks. We consider daytime and nighttime scenarios and investigate the effect of using RbFS, CsFS, or perfect clocks paired with SPADs or SNSPDs on the Allan deviation.

Figure 6(a) shows the overlapping Allan deviation [29] with channel conditions commensurate with a daytime space-to-Earth downlink utilizing adaptive optics (AO) wavefront correction. The red, green, and black curves correspond to RbFS, CsFS, and perfect clocks, respectively. The solid curves indicate SPADs, whereas the dashed curves indicate SNSPDs. The gray line is representative of a lower bound based on benign channel conditions and state-of-the-art (SOTA) clock components: $\eta_{ch} = -5.7$ dB, $N_b = 300$, $\Delta U = 3 \times 10^{-17}$, and $\sigma_U = 2 \times 10^{-16}$. The negative 1 slope indicates white phase modulation noise, which is consistent with the noise of frequency standards operated in phase-locked control loops [29,30]. The inset shows the relative timing stability for
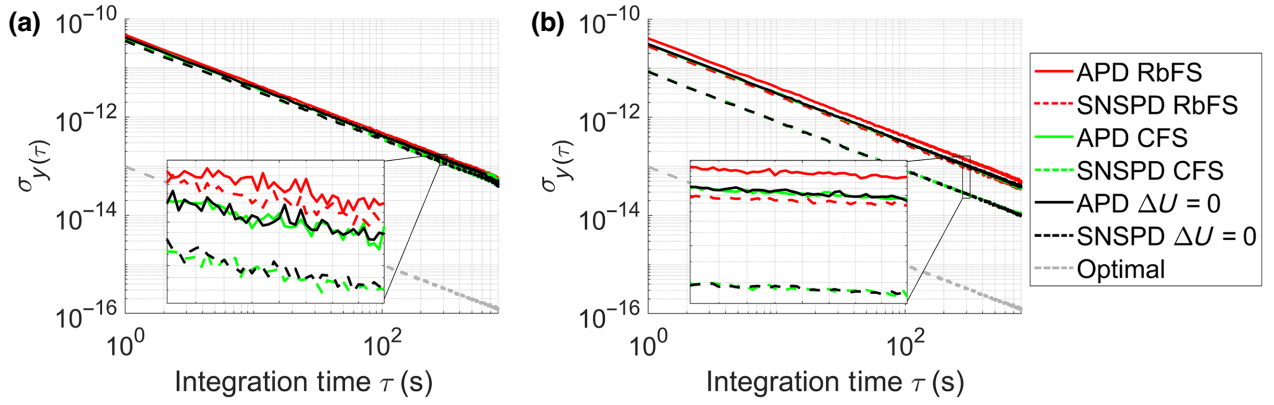
FIG. 6. The overlapping Allan deviation σ_y for channel attenuation $\eta_{ch} = -23$ dB and daytime (a) $N_b = 2.14 \times 10^6$ counts/s and (b) nighttime $N_b = 100 \times 10^3$ counts/s sky-background rates. The red, green, and black curves correspond to RbFS, CsFS, and perfect clocks, respectively. The solid curves indicate SPADs, whereas the dashed curves indicate SNSPDs. The gray line is representative of a lower bound based on benign channel conditions and SOTA clock components: $\eta_{ch} = -5.7$ dB, $N_b = 300$, $\Delta U = 3 \times 10^{-17}$, and $\sigma_U = 2 \times 10^{-16}$. The inset shows the relative timing stability for the different cases over the integration range from 280 to 320 s.

the different cases over the range of integration times from 280 to 320 s. As expected, there is an increase in stability as one uses detectors with less jitter and clocks with more stability. Reduced detector jitter results in smaller correlation widths σ_τ, which in turn causes smaller SEM $\sigma_{\bar{\tau}}$ and better stability. Interestingly, when using either SPADs or SNSPDs, switching from CsFSs to "perfect clocks" does not improve the stability. This shows that the detection jitter of SPADs or SNSPDs is the limiting factor when paired with clocks that are at least as stable as CsFSs.

Figure 6(b) shows the overlapping Allan deviation with channel conditions commensurate with a nighttime downlink utilizing AO. In this case the noise is reduced by a factor of about 21 and the increased signal to noise permits the scenario utilizing RbFS and SNSPDs (dashed red) to be comparable with the CsFS and SPAD case (solid green). Overall, this shows how one can explore the trade space of channel conditions and equipment specifications in order to meet a performance objective.

IV. RELEVANCE TO TELECOM CHANNELS

To demonstrate the applicability of our QTT algorithm and simulation, we first apply our results to a telecom-fiber channel. We do this by converting the channel attenuation η_{ch} to fiber length according to $\eta = -\alpha L$, where L is the total fiber length in kilometers and $\alpha = 0.22$ dB/km is the attenuation coefficient at 1550 nm. The result with $N_b \approx 10^3$ counts/s is shown in Fig. 7, where the probability of success P_s is plotted as a function of the total length of fiber between Alice and Bob. As expected, increasing the source heralding efficiency allows the QTT algorithm to perform better at longer fiber lengths. Furthermore, it shows that the QTT algorithm achieves high probability of success up to a

few hundred kilometers given the source rate and heralding efficiencies that we model.

V. RELEVANCE TO SPACE-EARTH CHANNELS

To further demonstrate the applicability of our QTT algorithm and simulation, we apply our results to channel conditions representative of a daytime space-to-Earth quantum downlink. We assume that a satellite in a 600-km circular orbit has a 15-cm transmit aperture and propagates 780-nm photons to a ground station with a 1-m receive aperture utilizing a 1-nm spectral filter. It is assumed that all the detectors in the system have efficiency $\eta_{det} = 0.6$, the spectral filters have efficiency $\eta_{spec} = 0.9$, and the ground station receiver has efficiency $\eta_{rec} = 0.5$. The angle-dependent atmospheric transmission efficiency η_{trans} and the background sky radiance H_b are generated in MODTRAN for a high desert climate with urban aerosols.

In Ref. [31] we established a theoretical framework in which the receiver performance is modeled as a function of atmospheric phenomena and AO system parameters. It uses scaling law equations to estimate the residual wavefront-phase error, after correction, and determine how the error inhibits the ability to transmit the signal light through a small spatial filter in the focal plane. In summary, the Greenwood frequency f_G characterizes the rate at which the turbulence is changing, and the Fried coherence length r_0 characterizes the spatial scale of the turbulence. The tip, tilt, and higher-order correction of an AO system counteract the negative effects of these phenomena. An AO system can be characterized by the closed-loop bandwidths of the system, the number of wavefront sensor subapertures, and the number of actuators making up the deformable mirror
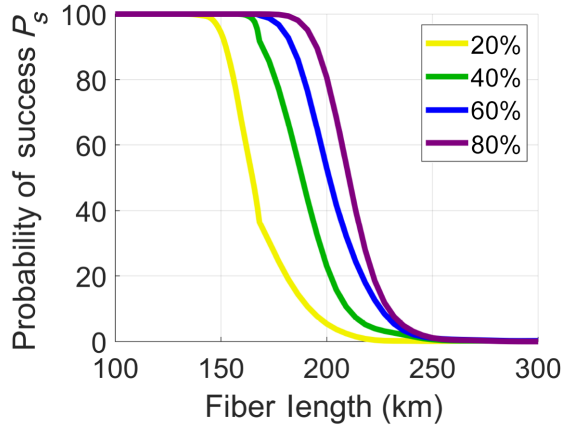
FIG. 7. The probability of success P_s as a function of the total length of fiber between Alice and Bob for a biphoton source with a 2-MHz pair rate and a background-photon rate of 1 kHz. The legend gives the heralding efficiency of the biphoton source.

(DM) that applies the correction. In the following subsections we are careful to present the residual errors that quantify the effect of these competing phenomena.

We consider two conservative cases for the optical receiver configuration. First, we assume that the receiver utilizes tracking alone, that is, only tip and tilt correction, with a tracking closed-loop bandwidth $f_{TC} = 50$ Hz. Secondly, we assume that the receiver is configured with both tracking and higher-order AO correction utilizing $N_{act} = 25$ mirror actuators and closed-loop bandwidth $f_c = 100$ Hz. In both cases, we use the aforementioned framework to map the results of our simulation to a daytime sky hemisphere to show the performance of the QTT algorithm for different heralding efficiency sources.

A. Tracking only

In the case of utilizing tracking alone, one can estimate the residual wavefront-phase error σ_ϕ as a combination of the error from the higher-order structure of the signal light [32] and the finite bandwidth of the tracking system [33]

$$\sigma_{\phi,CL}^2 = 0.582\left(\frac{D_R}{r_0}\right)^{5/3} + \left(\frac{\pi f_{TG}}{2 f_{TC}}\right)^2, \qquad (8)$$

respectively, where D_R is the diameter of the receiver aperture and f_{TG} is the tracking Greenwood frequency. This residual error is inserted in place of the terms in the brackets of Eq. A9 of Ref. [31], and the rest of the framework is unaltered, except for the zenith angle dependence of the atmospheric parameters [33].

Using this map, we are able to generate hemispherical plots for two sun positions and varying turbulence strengths. The plots show the regions where QTT succeeds with 99% probability, color coded by the heralding efficiency of the biphoton source. Given the aperture sizes

and channel conditions assumed, without higher-order AO, the signal attenuation will be significantly high with strong turbulence. Therefore, we assume a $1 \times \text{HV}_{5/7}$ Hufnagel-Valley turbulence profile [34], and investigate how changing the field of view (FOV) of the receiver changes performance. Intuitively, since the algorithm seems highly resilient to noise, a potential strategy is to open the FOV in order to reduce channel attenuation beyond the 99% threshold. The results are given in the downward progression in Figs. 8 and 9 where the FOV increases from $1\times$ to $3\times$ the diffraction-limited FOV. As one can see, increasing the FOV, which corresponds to a larger field stop in the focal plane, increases the sky hemisphere accessible by QTT, despite the increased probability of noise photons.

B. Tracking and higher-order AO

In the case of tracking and higher-order AO, one can estimate the residual error as a combination of the fitting error, aliasing error, and error due to the finite bandwidths of the tracking and higher-order AO systems [33],

$$\sigma_{\phi,CL}^2 = 1.3 \times 0.28\left(\frac{d_{sub}}{r_0}\right)^{5/3} + \left(\frac{\pi f_{TG}}{2 f_{TC}}\right)^2 + \left(\frac{f_G}{f_c}\right)^{5/3}, \qquad (9)$$

where d_{sub} is the subaperture spacing, which is matched to the DM actuator spacing, and the aliasing error is set to 30% of the fitting error. With AO, a stronger and more realistic daytime turbulence strength can be considered. In this case, we triple the turbulence strength by including a multiplicative factor on the turbulence profile, that is, we use a $3 \times \text{HV}_{5/7}$ Hufnagel-Valley profile [34]. We perform the same investigation as the previous case and open the FOV in two steps. Figures 10 and 11 give the results, showing the considerable boost in performance that AO supports even in the case of $3\times$ stronger turbulence. The results also show that good performance can be achieved using sources available today, which can have heralding efficiencies in the range of 20% to 40%, as long as AO is utilized.

In both cases, we have used conservative system parameters and restrictive constraints, e.g., 99% success probability, in order to demonstrate the utility of our methods. There is still quite a large trade space to be explored, and slight changes, for example larger aperture sizes, can make considerable changes to the results. Nonetheless, this framework can be used to model many different link conditions and the simulation results can be applied to different link budgets. A study exploring the extent to which opening the FOV is a suitable strategy should be included in any conceptual design. Some noteworthy concerns are the effects of the system dead time as the rates get extremely high and the structure of the turbulence-broadened photon-probability distribution at the spatial filter.
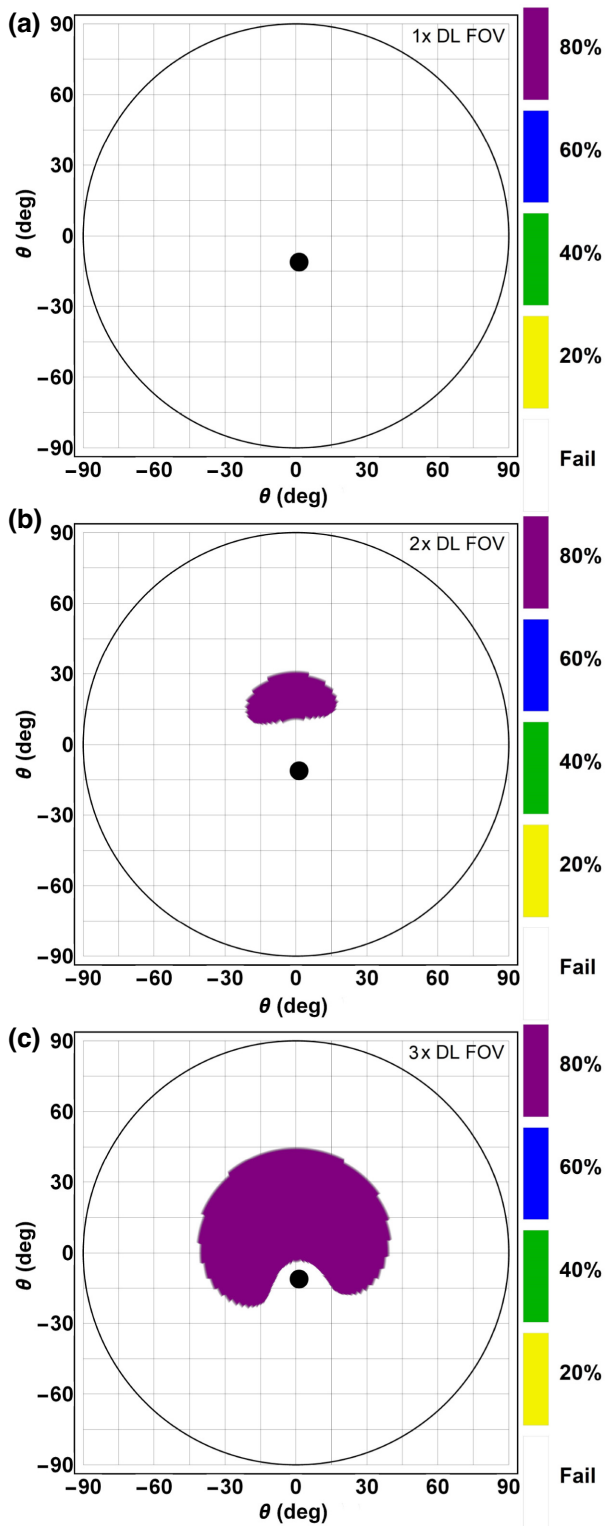
FIG. 8. Hemispherical plots of summer solstice with a $1 \times HV_{5/7}$ turbulence profile showing the regions where QTT succeeds with 99% probability for a receiver system with no higher-order AO (see Sec. V A for more details). The legend gives the heralding efficiency of the biphoton source. In (a)–(c) we enlarge the FOV from $1\times$ to $3\times$ the diffraction-limited (DL) FOV. The black dot represents the Sun's location.
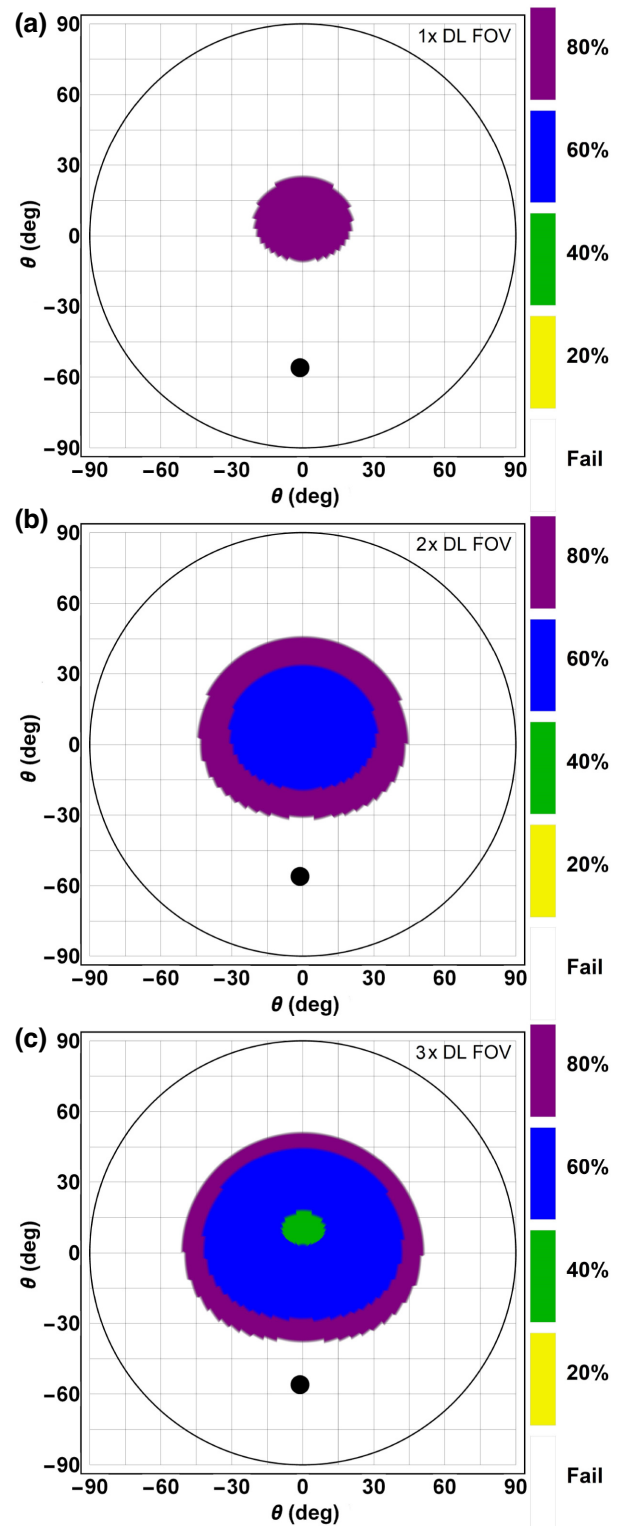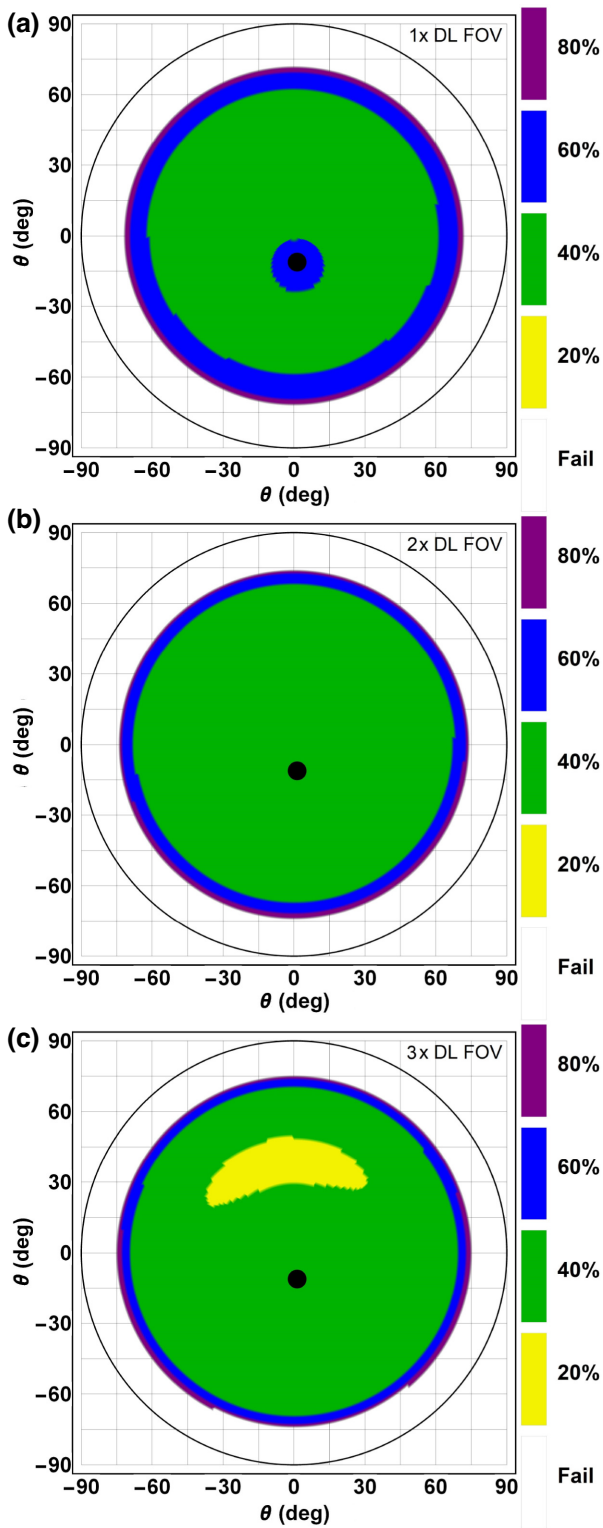
FIG. 9. Hemispherical plots of winter solstice with a $1 \times HV_{5/7}$ turbulence profile showing the regions where QTT succeeds with 99% probability for a receiver system with no higher-order AO (see Sec. V A for more details). The legend gives the heralding efficiency of the biphoton source. In (a)–(c) we enlarge the FOV from $1\times$ to $3\times$ the diffraction-limited FOV. The black dot represents the Sun's location.

FIG. 10. Hemispherical plots of summer solstice with a $3 \times HV_{5/7}$ turbulence profile showing the regions where QTT succeeds with 99% probability for a receiver system with higher-order AO (see Sec. V B for more details). The legend gives the heralding efficiency of the biphoton source. In (a)–(c) we enlarge the FOV from $1\times$ to $3\times$ the diffraction-limited FOV.
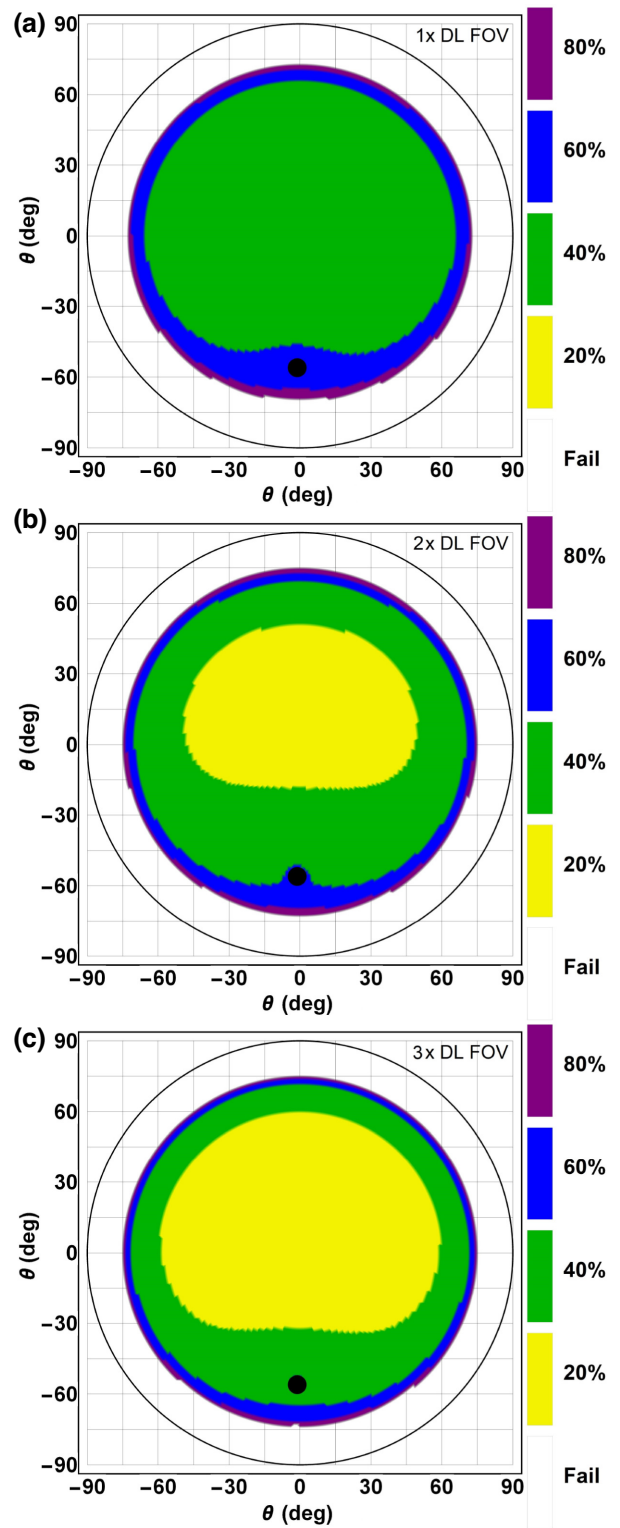

FIG. 11. Hemispherical plots of winter solstice with a $3 \times HV_{5/7}$ turbulence profile showing the regions where QTT succeeds with 99% probability for a receiver system with higher-order AO (see Sec. V B for more details). The legend gives the heralding efficiency of the biphoton source. In (a)–(c) we enlarge the FOV from $1\times$ to $3\times$ the diffraction-limited FOV.

VI. CONCLUSION

We investigate QTT as a candidate technique for the precise clock synchronization required to enable long-range daytime quantum networking and secure timing in GPS-denied environments. The architecture is simple and the algorithm is robust to signal loss and the presence of noise photons. We characterize the performance of QTT as a function of Bob's channel attenuation and the number of noise photons present in his channel. Our results can subsequently be used to determine performance for specific design references given a link budget has been carefully derived. We present the probability of successful time transfer and the standard error of the mean of the clock offset, which we show is the single-shot timing precision of the QTT algorithm. We further show that the standard error of the mean follows a $1/\sqrt{N_T}$ trend, where N_T is the estimate of the number of "true" coincidences between Alice and Bob. Setting a threshold probability of success to 99%, our results show how many noise photons can be present and how many true coincidences to expect given a certain channel loss. We also calculate the Allan deviation for different detection and clock systems, which conveys the stability and noise profile of the two-clock system. Finally, we interpret the results in the context of long fiber channels and daytime space-to-Earth downlinks, thereby demonstrating a specific design reference for the relevance of our method for global-scale quantum networking and timing in GPS-denied environments.

In this work we model the timing jitter associated with clocks and hardware. Thus, the results are valid for scenarios in which other deleterious effects have been modeled and compensated for, resulting in residual ΔU that is negligible. Future work should include estimates of the residual ΔU after compensating for relative motion, and jitter caused by atmospheric fluctuations in ground-space links. Similarly, future work could include modeling dispersion, temperature, and other effects unique to fiber networks. It would also be interesting to investigate the performance of our QTT algorithm in different configurations and across multiple nodes in a large network architecture including realistic channel conditions and hardware components as we have done in this work.

APPENDIX: ANALYTICAL MODEL

In this section we derive a model that predicts the performance of QTT based on parameters inferable from the channel conditions and hardware. Ultimately, we derive an expression for the probability of success as a function of the correlation signal peak height. We consider N_T photon pairs randomly and uniformly distributed in an acquisition time T_a. The detection time of each photon is randomized by the jitter of Alice's and Bob's detectors, which we model as a Gaussian random variable. Consequently, the detection-time difference histogram is a Gaussian with mean equal to the arrival time difference and standard deviation given by Eq. (7).

1. Clock drift

Next, we include the effect of the clock drift ΔU. We do this by dividing the acquisition time T_a into infinitesimal time increments dT. During each time increment the detection times of the photon pairs are Gaussian-distributed random variables with the same amplitude and standard deviation, but with center position shifted by $T\Delta U$. Thus, the coincidence signal can be modeled as

$$S = \frac{R_T}{\sigma_\tau \sqrt{2\pi}} \int_0^{T_a} \exp\left[-\frac{1}{2}\left(\frac{\tau - T\Delta U}{\sigma_\tau}\right)^2\right] dT, \quad (A1)$$

where R_T is the true coincidence rate. Integrating we find that

$$S = \frac{R_T}{2\Delta U}\left[\mathrm{erf}\left(\frac{\tau}{\sqrt{2}\sigma_\tau}\right) - \mathrm{erf}\left(\frac{\tau - T_a\Delta U}{\sqrt{2}\sigma_\tau}\right)\right]. \quad (A2)$$

To make this expression fit the simulation, or experimental results, one must accommodate for the effect of binning by multiplying Eq. (A2) by T_{bin}. As a check, taking the limit $\Delta U \to 0$, one appropriately finds

$$S(\Delta U \to 0) = \frac{R_T T_a}{\sigma_\tau \sqrt{2\pi}} \exp\left[-\frac{1}{2}\left(\frac{t}{\sigma_\tau}\right)^2\right], \quad (A3)$$

noting that the product $R_T T_a = N_T$ is the number of true coincidences. The expected number of detected true coincidences is

$$N_T = N_{\mathrm{pair}} \eta_{\mathrm{herald}}^2 \eta_A \eta_B \eta_{\mathrm{dead}}^A \eta_{\mathrm{dead}}^B, \quad (A4)$$

where η_{herald} is the heralding efficiency of the source, η_A and η_B are Alice's and Bob's channel efficiencies, and η_{dead}^A and η_{dead}^B are the efficiencies due to detector dead time.

Using Eq. (A2), we find the location and value of the signal peak

$$\tau_{\text{peak}} = \tfrac{1}{2} T_a \Delta U,$$

$$S_{\text{peak}} = \frac{N_{\text{T}}}{T_a \Delta U} \text{erf}\left(\frac{T_a \Delta U}{2\sqrt{2}\sigma_\tau}\right). \tag{A5}$$

Again, we can take the limit $\Delta U \to 0$ and appropriately find that

$$S_{\text{peak}}^{(\text{max})} \equiv S_{\text{peak}}(\Delta U \to 0) = \frac{N_{\text{T}}}{\sigma_\tau \sqrt{2\pi}}. \tag{A6}$$

Thus, we see that the effect of ΔU is to shift the peak and to reduce its height, which is detrimental to the precision and success probability of the QTT algorithm. Setting a threshold on the value of S_{peak}, perhaps based on the noise distribution, limits ΔU relative to the acquisition time and jitter of the system. For example, if one requires that S_{peak} be 99% of $S_{\text{peak}}^{(\text{max})}$ then

$$\Delta U \lessapprox \frac{1}{2} \frac{\sigma_\tau}{T_a}. \tag{A7}$$

If we assume SPAD detectors then ΔU should be less than 2×10^{-10} to meet the 99% $S_{\text{peak}}^{(\text{max})}$ threshold.

2. Probability of success

One way to derive the probability of success is to calculate the probability that a noise peak could be misidentified as the correlation peak. To do this, consider the background counts detected at Alice and Bob during the acquisition time T_a. The distribution of peak heights due to accidental coincidences has mean μ_b equal to the average number of accidental coincidences per time bin,

$$\mu_b = N_b^A N_b^B T_{\text{bin}}, \tag{A8}$$

where N_b^A and N_b^B are the observed background counts at Alice and Bob. We find that it is sufficient to approximate the noise peak distribution $f(s)$ by a Gaussian with mean μ_b and standard deviation $\sigma_b = \sqrt{\mu_b}$,

$$f(s) = \frac{1}{\sigma_b \sqrt{2\pi}} \exp\left[-\frac{1}{2}\left(\frac{s - \mu_b}{\sigma_b}\right)^2\right]. \tag{A9}$$

The probability that the peak is made up of accidental coincidences instead of the correlation signal is related to the nth-order statistic of the distribution of accidental peak heights $f(s)$,

$$f_n(s) = nF(s)^{n-1}f(s), \tag{A10}$$

where $F(s)$ is the cumulative distribution function (CDF),

$$F(s) = \frac{1}{2}\left[1 + \text{erf}\left(\frac{s - \mu_b}{\sqrt{2}\sigma_b}\right)\right], \tag{A11}$$

of the distribution of accidental peak heights $f(s)$. The order parameter n is related to the number of misidentification opportunities in the correlation histogram. The probability of success P_s is the probability that the largest peak due to accidental coincidences is less than the maximum peak of the correlation histogram S_{peak}. Mathematically, this is the CDF of the nth-order statistic $f_n(s)$ integrated to S_{peak},

$$P_s = \int_0^{S_{\text{peak}}} f_n(s)ds. \tag{A12}$$

Evaluating Eq. (A12) one finds that

$$P_s = 2^{-n}\left[\text{erfc}\left(\frac{\mu_b - S_{\text{peak}}}{\sqrt{2}\sigma_b}\right)^n - \text{erfc}\left(\frac{\mu_b}{\sqrt{2}\sigma_b}\right)^n\right]. \tag{A13}$$

Equation (A13) can be used to explain the shape of the contours in Fig. 3 in the following way. Inverting Eq. (A13) we find the threshold value of S_{peak}:

$$S_{\text{peak}}^{(\text{thresh})} = \mu_b - \sqrt{2\mu_b}\,\text{erfc}^{-1}\{[2^n(P_s + 2^{-n}\,\text{erfc}$$
$$(\sqrt{\mu_b/2})^n)]^{1/n}\}. \tag{A14}$$

Substituting Eqs. (A4), (A5), and (A8) into Eq. (A14) and solving for η_B, one can establish a function $\eta_B = \eta_B(P_s, N_b^B)$ and predict the shape of the contours in Fig. 3. Keeping the first two terms in a Taylor series expansion one finds an expression of the form

$$\eta_B = c_2\sqrt{N_b^B} + c_1 N_b^B, \tag{A15}$$

where

$$c_2 = -\frac{\sqrt{2N_b^A T_{\text{bin}}(T_a \Delta U)}\,\text{erfc}^{-1}(\mathcal{P}^{1/n})}{\mathcal{N}}, \tag{A16a}$$

$$c_1 = \frac{(N_b^A T_{\text{bin}})(T_a \Delta U)(\mathcal{P} - \exp[\text{erfc}^{-1}(\mathcal{P}^{1/n})]^2\mathcal{P}^{1/n})}{\mathcal{P}\mathcal{N}}, \tag{A16b}$$

$$\mathcal{N} = N_{\text{pair}}\eta_A\eta_A^{\text{dead}}\eta_B^{\text{dead}}\eta_{\text{herald}}^2\text{erf}\left(\frac{T_a \Delta U}{2\sqrt{2}\sigma_\tau}\right), \tag{A16c}$$

$$\mathcal{P} = 1 + 2^n P_s. \tag{A16d}$$

This analytical approach correctly predicts the overall shape observed from the Monte Carlo simulation, but it
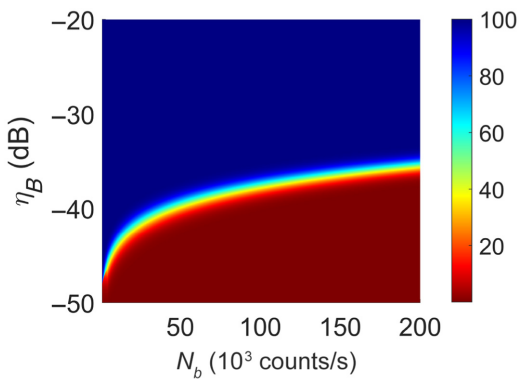
FIG. 12.   Analytical probability of success using Eq. (A13) and 40% heralding efficiency. See Fig. 3(b) in the main text for the corresponding simulation result.

generally overestimates the performance of QTT. In other words, the threshold attenuation predicted by Eq. (A15) is shifted downward compared to our simulation results. For example, in Fig. 12 we plot the analytical probability of success with 40% heralding efficiency. We choose the order parameter $n = 14$ and see that the analytical approach overestimates the performance by about 2 dB. The discrepancy suggests that the model may be incomplete. For example, the systematic steps of the proposed algorithm, such as the peak-finding process, are not accommodated for in the this model. Fundamentally, the signal peak height is simply *not* an unbiased estimator of the population peak height, which makes modeling the algorithm inherently problematic. Nonetheless, we find this progression useful because it justifies the fit used to trace out the 99% threshold curves in Fig. 3 in the main text and can be used to estimate performance.

[1] S. Wehner, D. Elkouss, and R. Hanson, Quantum internet: A vision for the road ahead, Science **362**, eaam9288 (2018).

[2] R. Van Meter, *Quantum Networking* (John Wiley & Sons, Hoboken, New Jersey, 2014).

[3] M. Aspelmeyer, T. Jennewein, M. Pfennigbauer, W. R. Leeb, and A. Zeilinger, Long-distance quantum communication with entangled photons using satellites, IEEE J. Sel. Top. Quantum Electron. **9**, 1541 (2003).

[4] K. Boone, J.-P. Bourgoin, E. Meyer-Scott, K. Heshami, T. Jennewein, and C. Simon, Entanglement over global distances via quantum repeaters with satellite links, Phys. Rev. A **91**, 052325 (2015).

[5] M. A. Lombardi, L. M. Nelson, A. N. Novick, and V. S. Zhang, Time and frequency measurements using the global positioning system, Cal Lab: Int. J. Metrol. **8**, 26 (2001).

[6] P. Exertier, E. Samain, N. Martin, C. Courde, M. Laas-Bourez, C. Foussard, and P. Guillemot, Time transfer by

laser link: Data analysis and validation to the ps level, Adv. Space Res. **54**, 2371 (2014).

[7] F. R. Giorgetta, W. C. Swann, L. C. Sinclair, E. Baumann, I. Coddington, and N. R. Newbury, Optical two-way time and frequency transfer over free space, Nat. Photonics **7**, 434 (2013).

[8] L. C. Sinclair, W. C. Swann, H. Bergeron, E. Baumann, M. Cermak, I. Coddington, J.-D. Deschênes, F. R. Giorgetta, J. C. Juarez, and I. Khader, *et al.*, Synchronization of clocks through 12 km of strongly turbulent air over a city, Appl. Phys. Lett. **109**, 151104 (2016).

[9] L. C. Sinclair, H. Bergeron, W. C. Swann, I. Khader, K. C. Cossel, M. Cermak, N. R. Newbury, and J.-D. Deschênes, Femtosecond optical two-way time-frequency transfer in the presence of motion, Phys. Rev. A **99**, 023844 (2019).

[10] W. C. Swann, M. I. Bodine, I. Khader, J.-D. Deschênes, E. Baumann, L. C. Sinclair, and N. R. Newbury, Measurement of the impact of turbulence anisoplanatism on precision free-space optical time transfer, Phys. Rev. A **99**, 023855 (2019).

[11] H. Dai, Q. Shen, C.-Z. Wang, S.-L. Li, W.-Y. Liu, W.-Q. Cai, S.-K. Liao, J.-G. Ren, J. Yin, and Y.-A. Chen, *et al.*, Towards satellite-based quantum-secure time transfer, Nat. Phys. **16**, 848 (2020).

[12] R. Quan, Y. Zhai, M. Wang, F. Hou, S. Wang, X. Xiang, T. Liu, S. Zhang, and R. Dong, Demonstration of quantum synchronization based on second-order quantum coherence of entangled photons, Sci. Rep. **6**, 1 (2016).

[13] A. Valencia, G. Scarcelli, and Y. Shih, Distant clock synchronization using entangled photon pairs, Appl. Phys. Lett. **85**, 2655 (2004).

[14] S. Haldar, I. Agullo, A. J. Brady, A. Lamas-Linares, W. C. Proctor, and J. E. Troupe, Towards global time distribution via satellite-based sources of entangled photons, Phys. Rev. A **107**, 022615 (2023).

[15] C. Ho, A. Lamas-Linares, and C. Kurtsiefer, Clock synchronization by remote detection of correlated photon pairs, New J. Phys. **11**, 045011 (2009).

[16] J. Lee, L. Shen, A. Cerè, J. Troupe, A. Lamas-Linares, and C. Kurtsiefer, Symmetrical clock synchronization with time-correlated photon pairs, Appl. Phys. Lett. **114**, 101102 (2019).

[17] M. Er-long, H. Zheng-fu, G. Shun-sheng, Z. Tao, D. Da-Sheng, and G. Guang-Can, Background noise of satellite-to-ground quantum key distribution, New J. Phys. **7**, 215 (2005).

[18] M. T. Gruneisen, M. L. Eickhoff, S. C. Newey, K. E. Stoltenberg, J. F. Morris, M. Bareian, M. A. Harris, D. W. Oesch, M. D. Oliker, and M. B. Flanagan, *et al.*, Adaptive-Optics-Enabled Quantum Communication: A Technique for Daytime Space-To-Earth Links, Phys. Rev. Appl. **16**, 014067 (2021).

[19] N. Ashby, Relativity and the global positioning system, Phys. Today **55**, 41 (2002).

[20] M. LLC, 5071A cesium primary time and frequency standard. https://www.microchip.com/en-us/products/clock-and-timing/components/atomic-clocks/atomic-system-clocks/cesium-time/5071a (2023).

[21] EverythingRF LLC, AXCS9000HP. https://www.every-thingrf.com/products/frequency-and-time-standards/axtal/914-1372-axcs9000hp (2023).

[22] L. Mandel and E. Wolf, *Optical Coherence and Quantum Optics* (Cambridge University Press, Cambridge, England, 1995).

[23] R. J. Glauber, Coherent and incoherent states of the radiation field, Phys. Rev. **131,** 2766 (1963).

[24] E. B. Rockower, Self-similarity and long-tailed distributions in the generation of thermal light, Am. J. Phys. **57,** 616 (1989).

[25] R. Schneider, C. Biernoth, J. Hölzl, A. Pscherer, and J. von Zanthier, Simulating the photon stream of a real thermal light source, Appl. Opt. **57,** 7076 (2018).

[26] A. Semenov and W. Vogel, Quantum light in the turbulent atmosphere, Phys. Rev. A **80,** 021802 (2009).

[27] G. F. Knoll, *Radiation Detection and Measurement* (John Wiley & Sons, Hoboken, New Jersey, 2010).

[28] A. W. Ziarkash, S. K. Joshi, M. Stipčević, and R. Ursin, Comparative study of afterpulsing behavior and models in single photon counting avalanche photo diode detectors, Sci. Rep. **8,** 5076 (2018).

[29] W. J. Riley and D. A. Howe, *Handbook of Frequency Stability Analysis* (US Department of Commerce, National Institute of Standards and Technology, Washington, DC, 2008).

[30] D. B. Sullivan, D. W. Allan, D. A. Howe, D. Sullivan, and F. Walls, *Characterization of Clocks and Oscillators* (National Institute of Standards and Technology Technical Note, Washington, DC, 1990).

[31] R. N. Lanning, M. A. Harris, D. W. Oesch, M. D. Oliker, and M. T. Gruneisen, Quantum Communication Over Atmospheric Channels: A Framework for Optimizing Wavelength and Filtering, Phys. Rev. Appl. **16,** 044027 (2021).

[32] R. J. Noll, Zernike polynomials and atmospheric turbulence, JOsA **66,** 207 (1976).

[33] J. W. Hardy, *Adaptive Optics for Astronomical Telescopes* (Oxford University Press on Demand, Oxford, England, 1998), Vol. 16.

[34] R. J. Sasiela, *Electromagnetic Wave Propagation in Turbulence: Evaluation and Application of Mellin Transforms* (Springer Science & Business Media, New York City, New York, 2012), Vol. 18, p. 5296227.